Towards improved reliability in the Infrared thermography simulations: calibrated modelling of a halogen heat source

by Van-Duong LE*, **, Luis ESPINOSA*, ***, Marie-Laetitia PASTOR*, ***, Marianne PERRIN*, ***, Yannick LE MAOULT****

* *Univ Toulouse, UTTOP, IMT Mines Albi, INSA Toulouse, ISAE-SUPAERO, CNRS, ICA, Tarbes, France.*
** *The University of Danang - University of Science and Technology, 54 Nguyen Luong Bang, 550000 Danang, Viet Nam.*
*** *University Institute of Technology of Tarbes, University of Technology Tarbes Occitanie Pyrénées UTTOP, 1 rue Lautréamont, 65000 Tarbes, France.*
**** *Univ Toulouse, IMT Mines Albi, INSA Toulouse, ISAE-SUPAERO, CNRS, ICA, Albi, France.*

Abstract

Halogen lamps are commonly used in active InfraRed Thermography (IRT). This study calibrates the spatial and temporal distributions of radiant heat flux from a halogen lamp and incorporates them into heat transfer models to assess the influence of the IRT measurement chain on an ABS plate. The results provide a comprehensive characterization of halogen lamp behaviour and establish reliable simulation boundary conditions. Validation using a pyrometer and IRT measurements, both calibrated against a blackbody, shows good agreement. These findings confirm the accuracy of the calibrated heat source and proposed models, improving fidelity for numerical defect detection and thermal processing applications.

1. Introduction

Infrared thermography (IRT) is a well-established Non-Destructive Testing (NDE) technique for inspecting and characterizing materials and structures, as it enables rapid, full field, and non-contact thermal measurements without damaging the object or generating hazardous radiation, making it highly suitable for structural health monitoring in various industrial applications [1]. In active IRT, an external thermal excitation is deliberately applied to the surface of a specimen, and the resulting transient temperature evolution is monitored using an infrared (IR) camera to reveal subsurface defects through thermal contrasts [2]. Over the past decades, significant progress in experimental configurations, excitation methods such as pulse, lock-in, and step heating thermography, and advanced signal processing techniques including phase analysis, thermal signal reconstruction, and machine learning approaches has greatly improved defect detectability, depth estimation, and noise reduction capabilities [3]. However, in active IRT tests, the measured thermal response originates not only from the inspected object but also from the external heat source, ambient reflections, atmospheric radiation, and internal noise generated by the infrared imaging system itself [4]. While thermal imaging can reveal the presence of potential issues in components and structures, the precise identification and characterization of specific damage mechanisms and subsurface defects remain challenging due to overlapping effects in the measurement chain, such as the characteristics of the heat source, heat transfer within the material, environmental conditions, the performance of the infrared detection system, and the subsequent data processing and interpretation steps [5]. Therefore, enhancing understanding on measurement chain, encompassing the heat source formation, propagation, detection, signal processing, and data interpretation, is essential. By isolating these effects through a combination of numerical and experimental approaches, it becomes possible to more accurately characterize flaws and classify their thermal signatures, thereby providing a foundation for distinguishing between different types of damage and defect characteristics. To address this, accurate heat source characterization is crucial, serving as the foundational link in the measurement chain.

Numerical simulation has become a powerful tool for analysing heat transfer mechanisms and supporting the interpretation of thermographic data, enabling detailed investigation of material properties, defect geometry, and testing parameters, as well as parametric studies that are difficult or costly to perform experimentally [6, 7]. However, achieving strong agreement between simulations and experiments remains challenging, partly due to simplified boundary conditions [8]. In particular, the external heat flux applied during excitation is often assumed to be spatially uniform and temporally constant, whereas real conditions involve complex distributions influenced by the heating source, surface properties, and environmental interactions such as convection and radiation, leading to errors in temperature predictions, thermal contrast, and defective estimations [2, 9]. Calibration of the external heat flux is therefore essential to improve the accuracy and reliability of simulations, especially when comparing different experimental setups or materials. Halogen lamps are commonly used as heat sources due to their performance and affordability, but many studies idealize their output as a spatially uniform over the specimen surface and temporally constant [10, 11]. In reality, halogen lamp radiant heat flux is non-uniform and affected by geometry, distance, emissivity, and environmental conditions, while transient intensity delays occur during switch-on and switch-off, all of

which directly affect thermal response and defect detectability [7, 12, 13]. To address this, theoretical Gaussian-type models and dedicated optical devices have been proposed to better characterize and control spatial distributions [9, 14], while predictive models rely on idealized heating functions that are iteratively refined based on validated experiments [10, 11, 15]. Nevertheless, these approaches lack direct empirical measurement and often fail to capture the actual non-linear temporal transients and spatial non-uniformities inherent to halogen lamps. This underscores the need for a direct, measurement-based heat flux characterization to ensure the fidelity of active IRT simulations.

This study presents an experimental characterization of the heat excitation emitted by a halogen lamp and the measured radiant heat flux, which is then incorporated into the development of 3D heat transfer models to account for the characteristics of the halogen lamp heat source and the influences of the measurement chain in active IRT. To achieve this, a thin film thermopile-based fluxmeter with a sensing area of 10 mm x 10 mm was employed to quantify the emitted heat flux at various distances and to assess its spatial sensitivity across the measurement surface. The fluxmeter sensor produces a voltage signal proportional to the incident thermal radiation and was previously calibrated using a radiative method based on blackbody radiation to ensure accurate heat flux measurements. The characterised excitation source is then integrated into heat transfer models for an Acrylonitrile Butadiene Styrene (ABS) plate. Finally, the simulation results are validated using both IRT and pyrometer measurements, which were pre-calibrated against a blackbody to provide reliable reference data for model validation. This coupled approach enables an assessment of the roles of the excitation source, propagation medium, and detection sensors within the thermal measurement chain. The present paper is organized as follows: Section 1 introduces the research context and objectives; Section 2 describes the experimental setup, including heat source calibration and numerical validation; Section 3 presents the 3D heat transfer model with geometry, boundary conditions, and mesh convergence; Section 4 discusses the results and comparisons between measurements and simulations; and Section 5 provides the concluding remarks.

2. Experiments

2.1. Calibration measurement tests of the heat excitation source

Figure 1 presents the layout used to measure the radiant heat flux emitted by a halogen lamp. The configuration includes a fluxmeter sensor employed to record the incident heat flux, which is connected to a data reading equipment used to process the electrical signals. Additionally, a motorized translation stage with a digital controller is integrated into the setup to precisely position the sensor and evaluate the spatial distribution of the thermal radiation. The fluxmeter is a thin film thermopile-based sensor with a sensing area of 10 mm by 10 mm (from NeoTIM, France). To ensure measurement precision, the sensor was specifically calibrated using a radiative technique involving thermal radiation from a blackbody source. This procedure demonstrated a linear relationship where the electrical output increased proportionally to the theoretical radiant heat flux from the blackbody and showed negligible variation across different calibration distances with a mean sensitivity of 0.56 ± 0.008 µV/(W/m²), confirming the high reliability of the sensor for the present measurements [16]. The signals were acquired using an HBM QuantumX MX840B data acquisition system with a temporal resolution of 0.1 second over a duration of 40 seconds. The sensor was mounted on a motorized three-axis positioning system (MISTRAS, France), which is digital controlled by a computer. A 500 W tubular halogen lamp with a 190 mm heating length was used as an external thermal excitation source. The lamp consists of a coiled tungsten filament encased in a quartz tubular enclosure. The spatial distribution of the heat flux

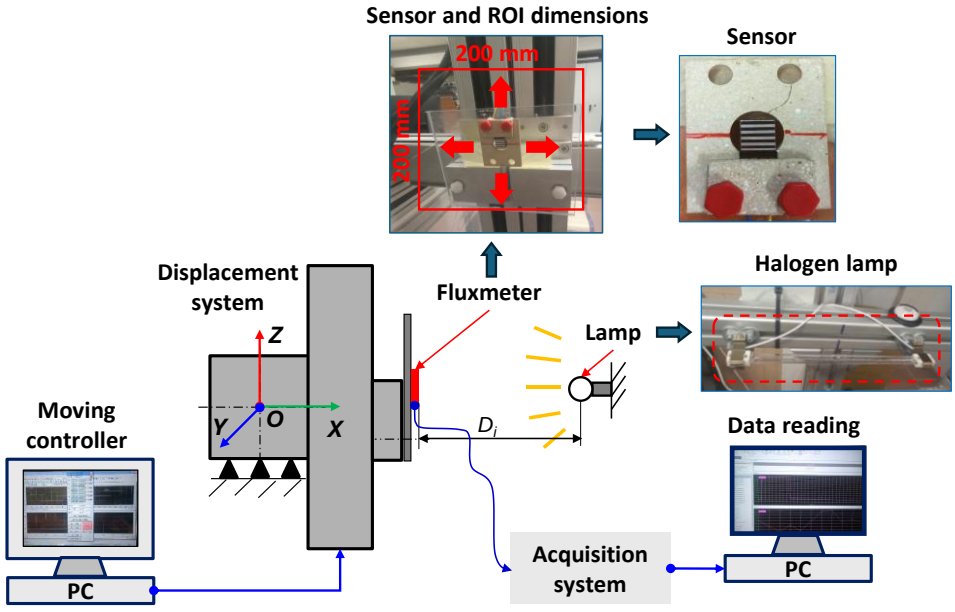

Figure 1. Testing setups used for the radiant heat flux measurement by using fluxmeter sensor.

was obtained by scanning a 200 × 200 mm² region of interest (ROI) cantered on the lamp, with a step size of 20 mm along both directions (Y and Z) at a distance of 60 mm from the source. A heating duration of 15 s was applied at each measurement position. This experimental procedure provides a detailed characterization of the spatial and temporal variations of the applied heat flux, which is provided in Section 4.1, enabling more realistic boundary conditions to be implemented in numerical models of active IRT.

2.2. Experimental validation of the numerical model

In this study, both pyrometry and IRT were employed to validate the simulation results, as shown in Figure 2, and the main characteristics of the devices used for the validation tests are summarized in Table 1. Pyrometers provide point-based temperature measurements, making them well suited for localized high-temperature monitoring, while IRT captures two-dimensional heat distributions, enabling analysis of the broader thermal field. The experimental results from both methods were compared to evaluate the influence of measurement techniques on thermal detection and to ensure reliable validation of the numerical simulations. A halogen lamp and a displacement system identical to those used in the previous tests were employed. An Acrylonitrile Butadiene Styrene (ABS) plate was selected as the test specimen due to its low thermal conductivity and well-defined thermophysical properties [17, 18], which promote slower heat diffusion and enhance transient thermal gradients, while its homogeneous and isotropic nature ensures uniform properties throughout the material, reducing uncertainties related to heterogeneity. The ABS plate, measuring 300 mm × 300 mm × 2.7 mm, was mounted on a frame at a distance of 60 mm from the lamp. The ROI on the plate surface measured 200 mm × 200 mm and was symmetrically aligned with the central section of the lamp, consistent with radiant heat flux calibration tests. For the pyrometry measurements, the pyrometer was mounted on the displacement system at distance of 500 mm to record temperatures at specific positions along the central section of the ROI, with each measurement repeated three times at 20 mm intervals. For the IRT tests, the IR camera was positioned 1100 mm from the specimen to capture the complete thermal response of the ROI, with each configuration tested in triplicate to ensure repeatability. The obtained data in the comparison with numerical results are represented in Section 4.2.

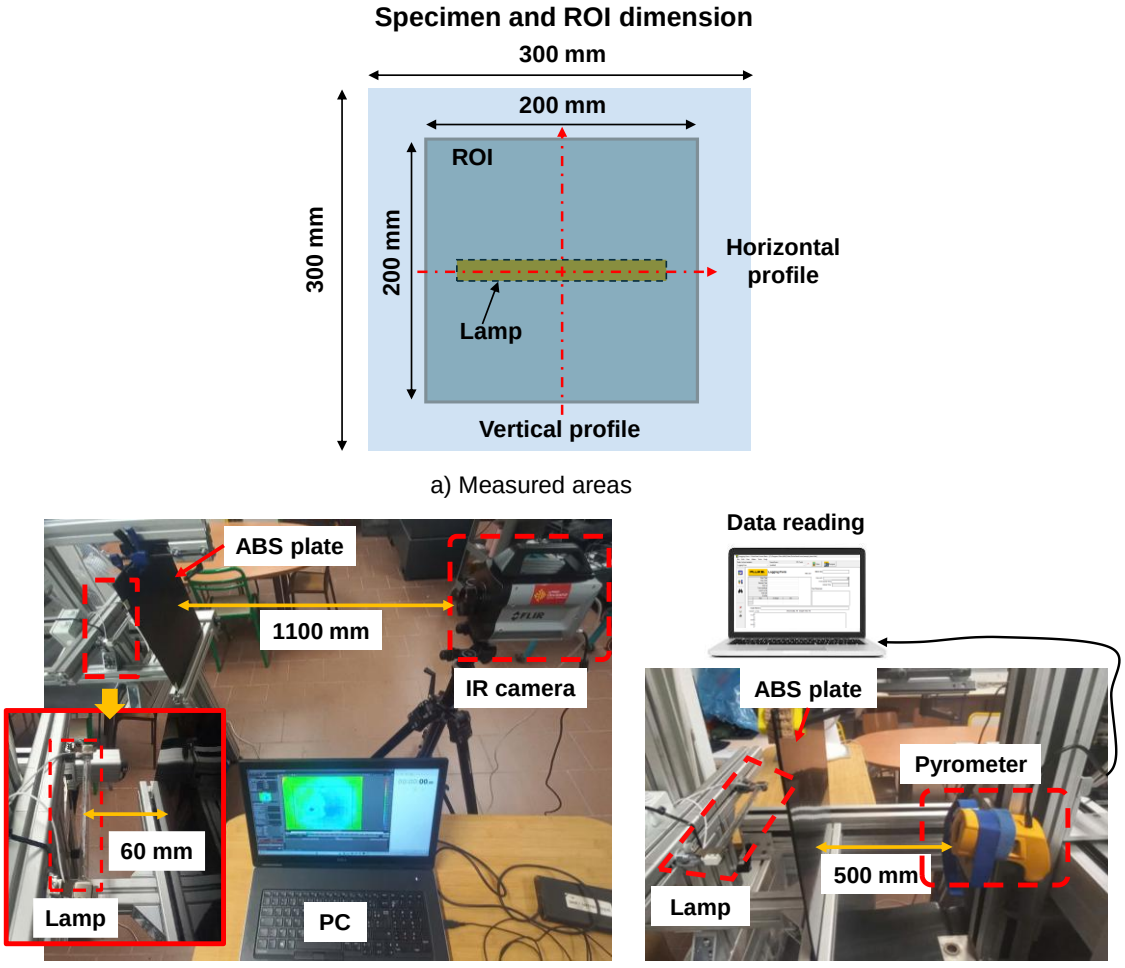

Figure 2. Measured areas (a) and setups used for tests using IR camera (b) and pyrometer (c).

Table 1. *IR camera and pyrometer characteristics used for validation tests.*

Devices	IR camera	Pyrometer
Model	A FLIR X6801sc MWIR (USA)	Fluke 572-2 model, USA
Characteristics	• 512 × 640 pixels; • NETD 20 mK. • MWIR (3-5 µm); • PC with ResearchIR Master software.	• Spectral response 8-14 µm; • Infrared accuracy of ±1% of the reading. • Resolution 0.1°C. • PC with FlukeView® Forms software.

3. 3D heat transfer models

3.1. Thermophysical parameters and boundary conditions

Multiphysics finite element simulations were conducted using COMSOL Multiphysics® to model the thermal response of an ABS plate with dimensions 200 mm × 200 mm × 2.7 mm, as shown in Figure 3. The simulation incorporated heat transfer mechanisms including conduction, convection, radiation, and external heat excitation, with each described by Eq. (1) to Eq. (4), respectively. Thermophysical parameters and material properties used in the model are summarized in Table 2. The ABS material was assumed to be opaque, with constant thermophysical properties that remain independent of the low temperature range considered [9, 15].

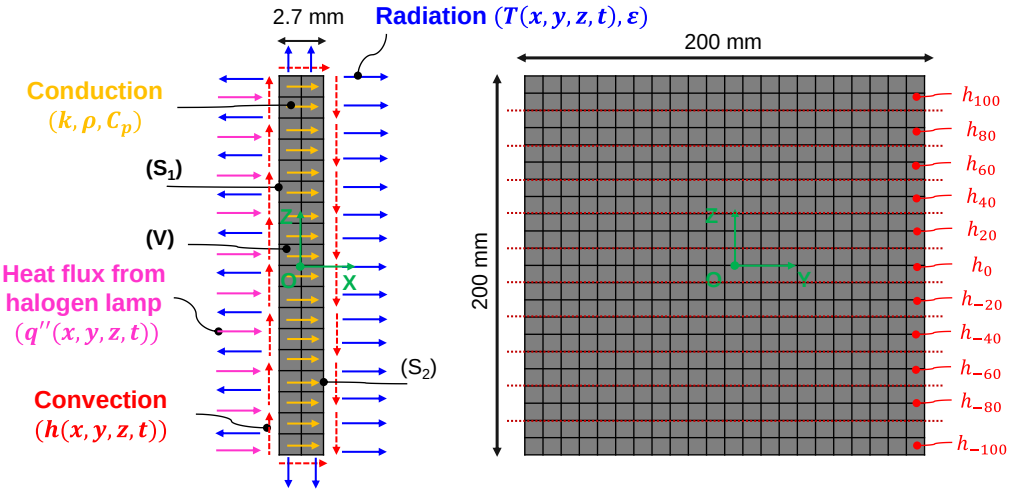

Figure 3. Layout of the setup used for simulation where yellow, red, blue, and pink arrows denote the mechanisms of conduction, convection, radiation, and external applied heat flux respectively, with convection and radiation boundary conditions applied to all exposed surfaces.

$$\rho C_p \frac{\partial T}{\partial t} = \nabla \cdot (k \nabla T) + Q, \quad \forall M \in V \tag{1}$$

$$-n \cdot (-k \nabla T) = h(x,y,z,t).(T - T_\infty), \quad \forall M_S \in V \tag{2}$$

$$-n \cdot (-k \nabla T) = \varepsilon \sigma (T^4 - T_{amb}^4), \quad \forall M_S \in V \tag{3}$$

$$-n \cdot (-k \nabla T) = q''(x,y,z,t), \quad \forall M \in S_1 \tag{4}$$

Here, ρ, C_p, k, T, Q, and t material density, specific heat capacity, thermal conductivity, temperature, internal heat generation per unit volume, and elapsed time (s), respectively. M is a point within the specimen volume V, while M_S represents a point located on all exposed surfaces of the specimen. In this study, no internal heat generation occurs, therefore Q is set to zero. The simulation starts with a uniform initial temperature equal to the ambient laboratory temperature, $T_{amb} = 292.15\,[K]$. For the convection process, $h(x,y,z,t)$ represents the convective heat transfer coefficient, which depends on time and the specimen surface location [16]. The inward conductive heat flux is expressed by $-n \cdot (-k \nabla T)$ according to Fourier's law, and ε is the emissivity of the ABS plate. External heat excitation from the halogen lamp is applied on surface S_1, with $q''(x,y,z,t)$ describing its spatially and temporally varying

distribution obtained from previous experiments. Each heating phase lasts 15 seconds, followed by a cooling period, and the complete test is simulated over a total duration of 400 seconds.

Table 2. *Thermal properties of ABS material used for simulation.*

Parameters	Values	Sources
Density, ρ [kg/m3]	1050	[17, 18]
Specific heat capacity, C_P [J/ (kg. K)]	1680	
Emissivity, ε	0.94	
Thermal conductivity, k [W/ (m. K)]	0.194	[16]
Convective heat transfer coefficient, h [W/ (m2. K)]	$h(x, y, z, t)$	

3.2. Mesh element size resolutions

A series of tests was subsequently conducted to evaluate mesh convergence with respect to element size. The spatial resolution of the mesh elements in all three directions was considered, including the incident surfaces in the YZ plane and the plate thickness in the X direction, characterized by the number of mesh layers. In YZ plane, the mesh element size was gradually reduced from 20 mm x 20 mm to 0.6 mm x 0.6 mm. It is noted that minimum mesh resolution was selected to align with the projected pixel size of the IR camera within the ROI. For X direction, the number of mesh layers was increased from 1 to 5 to achieve a cubic element shape at the smallest size. The influences of mesh resolutions on central section profiles at t = 5s are shown in Figure 4. The results indicate that temperature values are sensitive to mesh density, decreasing as the element size is reduced and the layer count increases, and become consistent when the mesh size is smaller than 5 mm x 5 mm with at least 3 layers. A summary of the extended test results is presented in Figure 5. Figure 5a presents the total number of Degrees of Freedoms (DOFs) for each mesh configuration. The DOFs increases significantly when decreasing the mesh element size from 2 mm to 0.6 mm. Notably, the number of DOFs is proportional to both the computational time and the required hardware resources [16]. Figure 5b shows the maximum relative errors of the temperature distributions for various element size models compared to the reference case of 0.6 mm. The error decreases as the mesh element sizes are reduced. The model with an element size of 2 mm x 2 mm and 3 layers shows a negligible error of less than 0.2% compared to the reference case. Therefore, this configuration was selected as it provides an optimal balance between accuracy and computational efficiency. The final computational model includes approximately 5.1×10^5 DOFs, requires 11 GB of virtual memory. The simulation was computed on a system equipped with an Intel Xeon® W7-3555 processor and 256 GB of RAM, taking about 3 hours to complete.

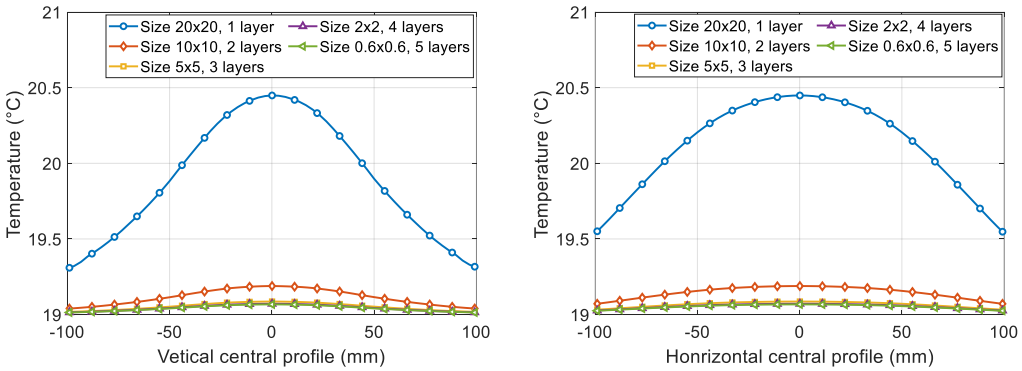

Figure 4. Temperature distributions on vertical (left) and horizontal (right) central profiles at t = 5s.

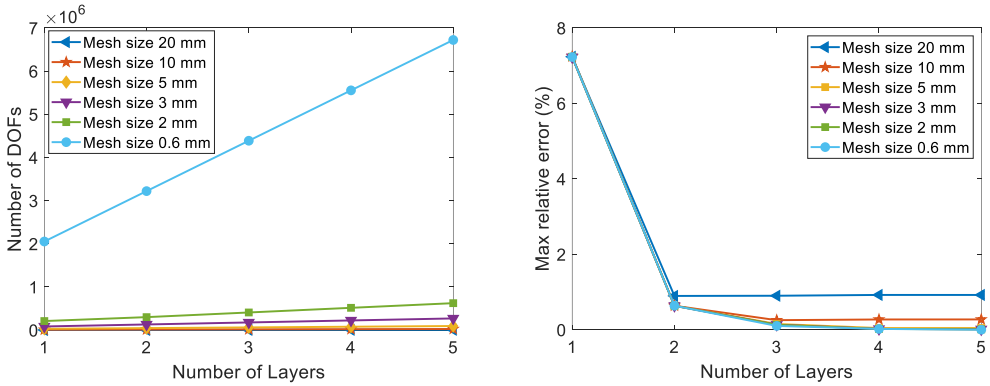

Figure 5. Computational resource (left) and max relative error (right) with mesh element size.

4. Results and discussion

4.1. Characterisations of the radiant heat flux emitted by a halogen lamp

The characteristics of the measured radiant heat flux at the central position of the lamp for various distances are shown in Figure 6a, while Figure 6b presents the heat flux distribution along the central section of the ROI, cantered under the halogen lamp at a distance of 60 mm. The measured heat flux represents a spatial average over the sensor active area of 10 mm by 10 mm at each location. At each distance, three consecutive measurements were performed with a standard variation of less than 0.8%, confirming high reproducibility. It can be seen that the radiant heat flux decreases rapidly with increasing observation distances (D_i). The attenuation behaviours of radiant heat flux following a power-law decay with a fitted exponent of 1.6, which is slightly lower than the theoretical inverse-square law of geometric spreading, reflecting the cumulative impacts of actual ambient conditions, expressed in Eq. (5). The heat flux along the central section profile is maximized at the lamp centre and distributed symmetrically, forming a pronounced peak with steep gradients toward the edges. Comparison between vertical and horizontal profiles shows that the vertical distribution is more focused with a sharper peak, whereas the horizontal distribution is broader and more diffuse. This distribution can be described by a Gaussian-like profile [9], expressed by the fitted function in Eq. (6). Here, $A(D_i)$ is the peak heat flux determined based on Eq. (5), l_{Pr} is the profile length (mm), C is a constant equal to 106 and 140 for vertical and horizontal profiles, respectively.

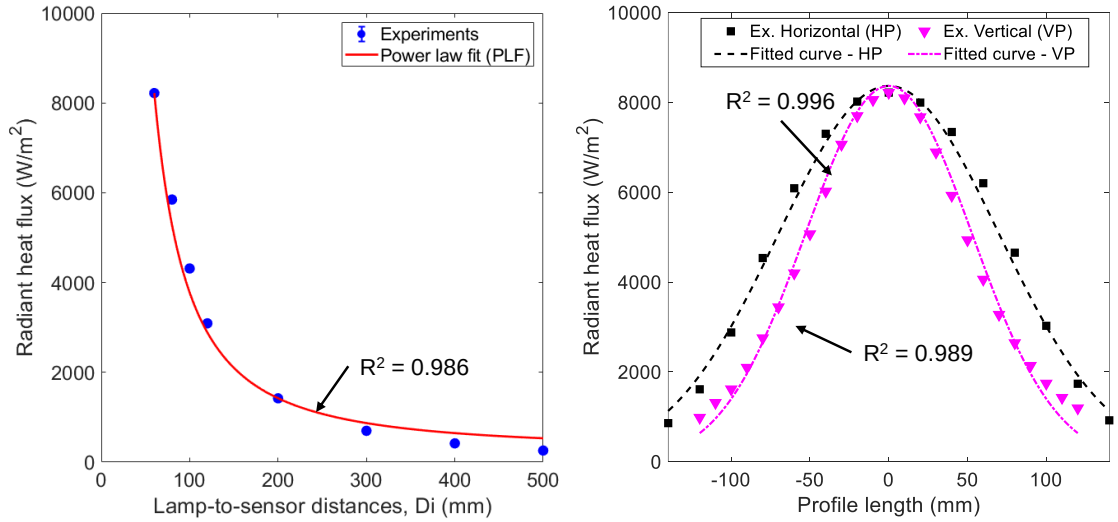

Figure 6. Characteristics of the radiant heat flux emitted by the halogen lamp at centre (left) and along the central section profiles at a distance of 60 mm (right).

$$PLF(D_i) = 264.3 + \frac{5567582}{D_i^{1.6}} \quad (5)$$

$$q''(D_i, l_{Pr}) = A(D_i) + \exp\left(\frac{2l_{Pr}^2}{C^2}\right) \quad (6)$$

Figure 7a and Figure 7b show the spatial and temporal distributions of the radiant heat flux over the full measured surface at a distance of 60 mm, respectively. On the one hand, the results revealed a strongly non-uniform power density across the ROI, following a Gaussian-like distribution with a peak at the centre and a rapid decrease toward the edges [9]. This steep gradient indicates that most of the radiative energy is concentrated within a limited central region. On the other hand, the results of the temporal distribution of the radiant flux confirms that halogen lamps exhibit a slight on/off switching delay when transitioning from the off state to full power, resulting in a short lag before reaching a steady radiant heat flux [12, 13]. In the duration under a 15 second pulse heating condition in the present study, immediately after switching on, the heat flux rises rapidly, then increases more gradually and reaches approximately 100% after 9 seconds, achieving maximum intensity. Following switch-off, the heat flux drops sharply within 2 seconds and then gradually decreases to ambient conditions. The first stage is attributed to the rapid cooling of the tungsten filament while the subsequent gradual decrease is governed by the thermal inertia of the quartz tube which continues to radiate heat for an extended period [12, 19]. This behaviour may also be influenced by external factors such as the physical proximity between the fixing sensor structures and the lamp which can create thermal confinement and restrict the natural cooling rate, making the accurate determination of the radiant heat flux for specific conditions crucial. These observations confirmed that the thermal energy emitted by the halogen lamp exhibits a time-dependent variation, rather than remaining strictly constant [11, 12]. These findings provide essential information for boundary condition setups in active IRT simulation to enhance accuracy and reliability of numerical results.

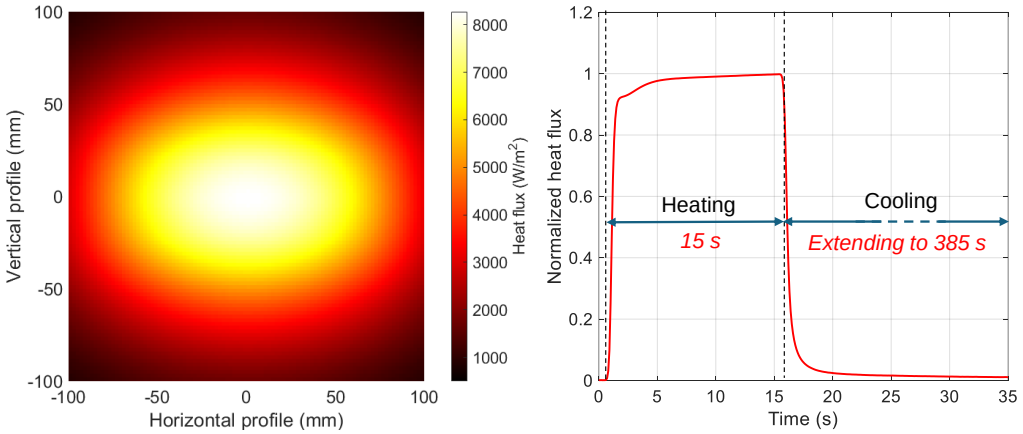

a) Heat flux distribution b) Time-dependent function

Figure 7. Distributions of radiant heat flux at the distances of 60 mm.

4.2. Validated numerical results

4.2.1. Influences of temperature measurement methods

Both the pyrometer and IR camera were used to measure the calibrated temperature of a blackbody to access the influence of environmental conditions and spectral response discrepancies at current experimental conditions. Both devices were set at same distance, ensuring full capturing of the aperture size 101.6 mm x 101.6 mm of the blackbody (model SR − 800R, Artisan Technology Group, USA). The ambient temperature during these tests is 22.5 °C, with detailed setups provided in [16]. The temperature profile in the horizontal profile of blackbody aperture is shown in Figure 8 and Figure 9, at distances of 430 mm and 1630 mm, respectively, for nominal settings of 15 °C, 25 °C, and 40 °C, which represent conditions below, near, and above the surrounding environment temperature respectively. At distance of 430 mm, as presented in Figure 8, it can be seen that the aperture edges function as a thermal transition zone where the temperature is influenced by the surrounding environment. This interaction leads to a marginal thermal non-uniformity across the aperture, which becomes more observable, at around 0.1 °C (max relative homogeneity error of 0.4%), as the gap between the heat source value and the surrounding temperature increases. A comparison at the aperture centre, which was also measured by the pyrometer with a laser spot size of 20 mm, shows a significant difference in accuracy. The relative errors were 1.7 %, 3.2 %, and 3 % for the IR camera, compared to 1.3 %, 0.8 %, and 0.3 % for the pyrometer relative to the nominal settings. In addition, increasing the distance between the measurement equipment and the blackbody significantly affected the temperatures obtained by the IR camera, as shown in Figure 9. This effect can be attributed to atmospheric interaction and the increasing contribution of the surrounding environment within the camera's field of view. When the heat source temperature is lower than the ambient temperature, radiation from the surroundings and intervening air leads to an overestimation of the measured temperature. Conversely, when the heat source temperature is higher than the ambient temperature, the measured temperature decreases with distance due to attenuation and mixing with cooler ambient radiation. At a distance of 1630 mm, the total relative error for the IR camera increased to 4.5 %, while the pyrometer error remained less than 1 %. These results highlight that IR camera measurements are more sensitive to distance-related effects such as atmospheric absorption, emission, and field-of-view averaging, whereas the pyrometer remains comparatively less affected due to its localised and narrower measurement spot and reduced environmental influence [16].

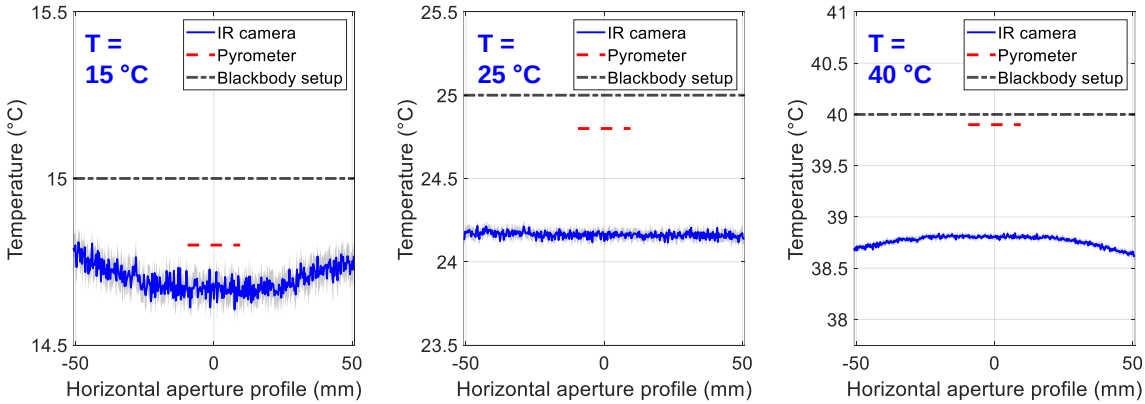

Figure 8. Temperature distributions in horizontal profile of the blackbody aperture at distance of 430 mm.

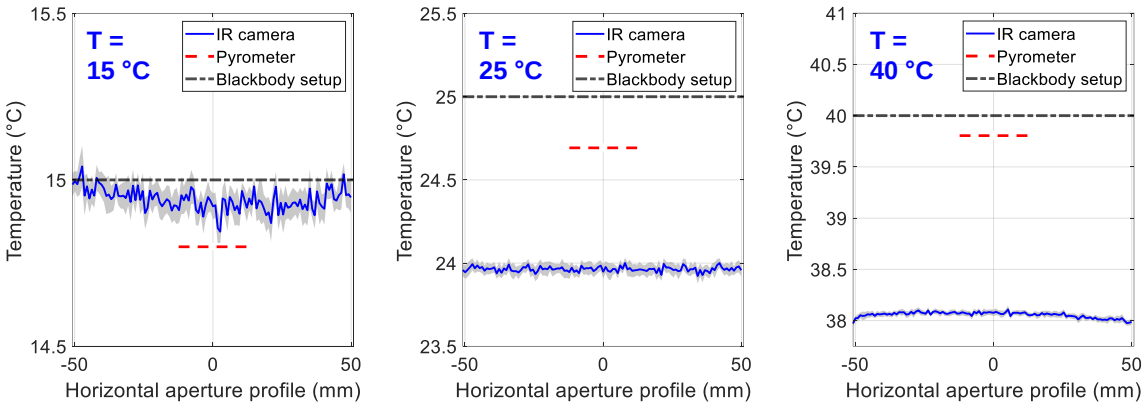

Figure 9. Temperature distributions in horizontal profile of the blackbody aperture at distance of 1630 mm.

4.2.2. Validated results on specimen central section profiles

Figure 10 presents the validation of numerical temperature distributions along the central section profile at 40 s, 100 s, 200 s, and 300 s from the start of the experiment, capturing the transient thermal behaviour during the cooling phase based on both IR camera and pyrometer measurements. The temperature profiles exhibit maximum values at the centre and a gradual decrease toward the plate edges, following a Gaussian-like distribution. The peak temperature reaches approximately 40 °C at the end of heating and decreases progressively during cooling. While the horizontal profile remains nearly symmetric over time, the vertical profile changes significantly over time due to an upward shift of the heat-affected region, mainly attributed to the natural rise of hot air after heating and the limited space for cooling. This leads to non-uniform convective behaviour along the vertical axis. To account for this, the local heat transfer coefficients were calculated at various positions using the lumped capacitance method based on measured pyrometer data [16]. This approach serves as an effective inverse method to determine the heat exchange parameters which represent a global heat transfer coefficient combining both convective and radiative components. Applying these experimentally derived coefficients into the boundary conditions significantly improves the accuracy of the simulated thermal response during the cooling phase.

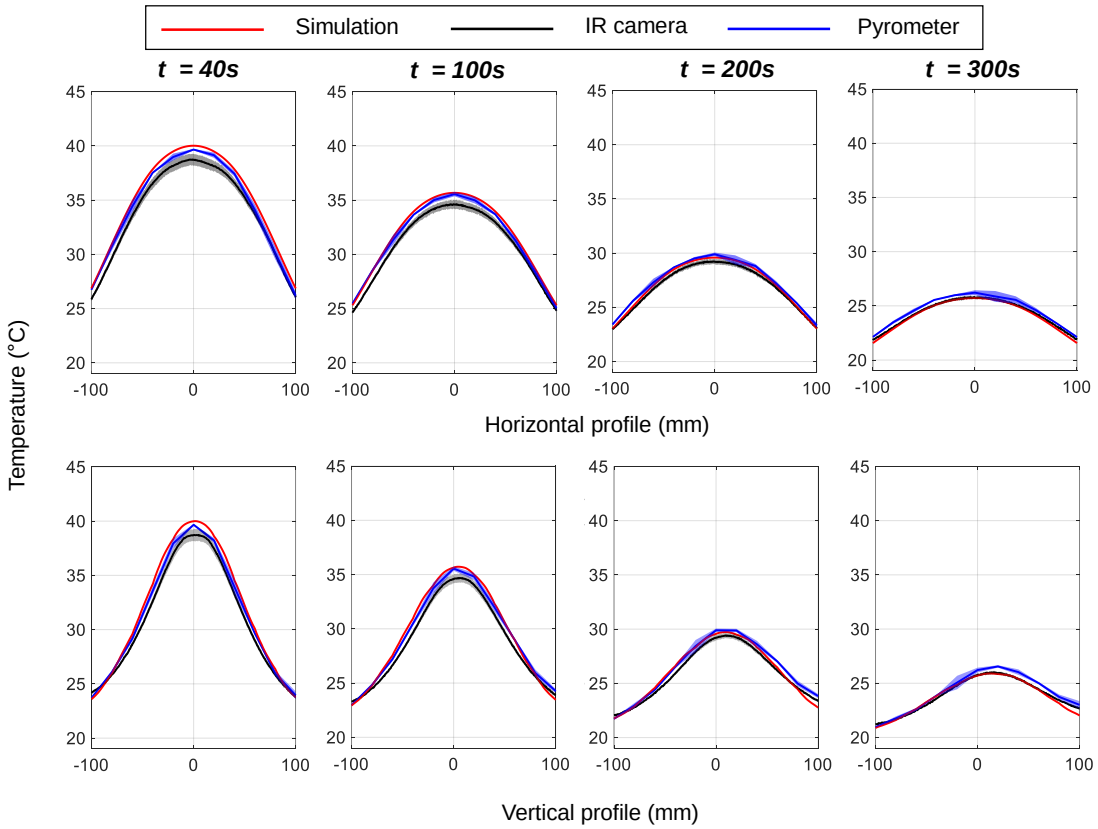

Figure 10. Validated results in central cross section profile at heat source distance of 60 mm.

The maximum relative temperature errors between the simulated and measured central section profiles over the full cooling duration are presented in Figure 11. The simulation shows strong agreement with experimental results for both measurement methods, with the max numerical relative error remained below 4% compared with pyrometer measurements and below 6% compared with IRT results. This difference can be attributed to the nature of the measurement techniques, as IRT provides full-field thermal monitoring and is more sensitive to spatial resolution and environmental conditions, whereas the pyrometer offers more stable, localized point measurements. These results confirm the accuracy and reliability of the numerical model in capturing transient thermal behaviour, supported by well-defined thermophysical parameters, numerical boundary conditions, discretization convergence, and the halogen lamp excitation source characterisation.

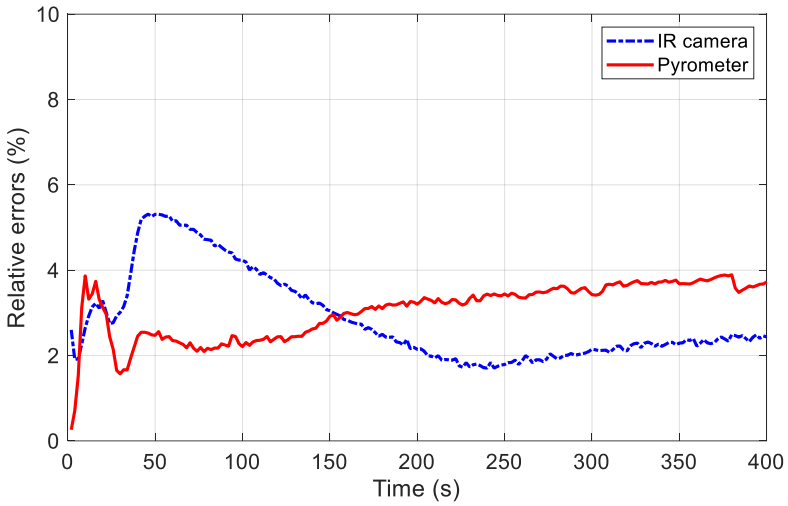

Figure 11. Max relative errors calculated on central section profiles.

5. Conclusion

This study focused on the experimental characterization of radiant heat flux from a halogen lamp and its integration into a 3D heat transfer model for considering the influence of the IRT measurement chain. Experimental measurements of the radiant heat flux from a halogen lamp revealed a pronounced distance-dependent decay consistent with a power law, alongside a highly non-uniform spatial distribution following a Gaussian-like profile, reflecting the combined effects of the lamp geometry and actual ambient conditions. Furthermore, the lamp exhibited a slight thermal response delay when transitioning between the off state and full power, and vice versa. These results highlight the importance of accurately representing heat source characteristics in thermal simulations. The developed multiphysics model was validated using both pyrometer and IR camera measurements, with both devices demonstrating high precision following blackbody calibration. While the pyrometer provided more accurate temperature readings at specific points and localised small spot size, the IR camera's accuracy decreased as the observation distance increased due to its sensitivity to environmental and spatial factors. The comparison between simulation and experimental results showed strong agreement in temperature distribution. These findings confirm the accuracy of the radiant heat flux characterization, ensuring the reliability of the thermophysical parameters, numerical boundary conditions and discretization convergence. This comprehensive characterization has enhanced the understanding of heat flux characteristics, material thermal response, and the factors influencing thermal measurements.

Overall, the proposed approach enhances the reliability and physical realism of thermal simulations by incorporating experimentally measured heat flux conditions rather than relying on idealized assumptions. By integrating real heat source data, the model provides a more accurate representation of heat transfer mechanisms involved in active IRT. These findings are particularly promising for numerical applications in defect detection and thermal processing fields. Moreover, this study establishes a solid foundation for future work toward a fully integrated simulation framework incorporating the complete measurement chain to improve accuracy and reduce the gap between numerical and experimental results. Future research should integrate IR camera characteristics, including radiometric calibration, pixel-level spatial averaging, optical transfer effects, detector noise, temporal response, and environmental interactions, to enhance physical consistency and improve the predictive capability of active IRT-based numerical models.

Acknowledgments

We would like to sincerely thank Dr. Rémi GIBLAS, Research Engineer, and Mr. Adrien LIEUREY, Technician at the Institut Clément Ader (ICA), École Nationale Supérieure des Mines d'Albi-Carmaux (IMT Mines Albi), for their support in the sensor calibration process. We also thank Mr. Gaël USTAZE, Technician at the GMP Department, IUT de Tarbes, Université de Technologie Tarbes Occitanie Pyrénées (UTTOP), for his support in the experimental setups.

References

[1] Y. Wu, M.-L. Pastor, M. Perrin, P. Casari, and X. Gong, «A new methodology to predict moisture effects on mechanical behaviors of GFRP-BALSA sandwich by acoustic emission and infrared thermography,» Composite Structures, vol. 287, pp. 115342, 2022.

[2] S. S. Pawar and V. P. Vavilov, «Applying the heat conduction-based 3D normalization and thermal tomography to pulsed infrared thermography for defect characterization in composite materials,» International Journal of Heat and Mass Transfer, vol. 94, pp. 56–65, 2016.

[3] H. Tuo, L. Wang, J. Zhang, X. Zhang, S. Dong, and X. Li, «The defect quantification in additive manufacturing composites using fused infrared thermography and artificial intelligence,» Composites Part B: Engineering, vol. 309, pp. 113114, 2026.

[4] T. Sosnowski, M. Kastek, G. Bieszczad, S. Gogler, B. Więcek, R. Strąkowski, and M. Felczak, «Method and test stand for calibrating the thermal imaging camera," in Proceedings of the 2022 International Conference on Quantitative InfraRed Thermography, QIRT Council, 2022.

[5] S. Lee, Y. Chung, C. Kim, and W. Kim, «Image segmentation for automatic detection and detectability evaluation of thinning defects using LSM-based induction thermography,» Infrared Physics & Technology, vol. 134, pp. 104900, 2023.

[6] V. P. Vavilov, A. O. Chulkov, V. V. Shiryaev, M. V. Kuimova, and H. Zhang, «Noise suppression in pulsed IR thermographic NDT: Efficiency of data processing algorithms,» NDT & E International, vol. 148, pp. 103240, 2024.

[7] B. Cosson, F. Schmidt, Y. Le Maoult, and M. Bordival, «Infrared heating stage simulation of semi-transparent media (PET) using ray tracing method,» International Journal of Material Forming, vol. 4, pp. 1–10, 2011.

[8] M. S. Carvalho, A. P. Martins, and T. G. Santos, «Simulation and validation of thermography inspection for components produced by additive manufacturing, » Applied Thermal Engineering, vol. 159, p. 113872, 2019.

[9] F. Lopez, V. De Paulo Nicolau, C. Ibarra-Castanedo, and X. Maldague, «Thermal–numerical model and computational simulation of pulsed thermography inspection of carbon fiber-reinforced composites,» International Journal of Thermal Sciences, vol. 86, pp. 325–340, 2014.

[10] H. V. Silva, A. P. Martins, M. A. Machado, T. G. Santos, and M. S. Carvalho, «Double active thermographic inspection of additive manufacturing composites: numerical modelling and validation,» Measurement, vol. 218, pp. 113212, 2023.

[11] V. P. Vavilov, D. D. Burleigh, A. O. Chulkov, and D. Y. Kladov, «Simulated delaminations in thermal NDT standards and the concept of thermally equivalent defects,» NDT & E International, vol. 151, pp. 103278, 2025.

[12] H. Plasser, G. Mayr, G. Mayr, G. Hendorfer, and Z. Major, « Enhanced photothermal parameter estimation of thick CFRP in reflection mode for rectangular pulse excitation by Halogen lamps,» Infrared Physics & Technology, vol. 118, p. 103911, 2021.

[13] S. Wu, B. Gao, Y. Yang, Y. Zhu, P. Burrascano, S. Laureti, M. Ricci, and Y. Wang, «Halogen optical referred pulse-compression thermography for defect detection of CFRP,» Infrared Physics & Technology, vol. 102, p. 103006, 2019.

[14] M. Barus, H. Welemane, F. Collombet, M. L. Pastor, A. Cantarel, L. Crouzeix, Y. H. Grunevald, and V. Nassiet, «Bonded repair issues for composites: An investigation approach based on infrared thermography,» NDT & E International, vol. 85, pp. 27–33, 2017.

[15] M. Grosso, J. E. C. Lopez, V. M. A. Silva, S. D. Soares, J. M. A. Rebello, and G. R. Pereira, «Pulsed thermography inspection of adhesive composite joints: computational simulation model and experimental validation,» Composites Part B: Engineering, vol. 106, pp. 1–9, 2016.

[16] V.-D. Le, L. Espinosa, M.-L. Pastor, M. Perrin, and Y. Le Maoult, «Heat transfer modelling of radiant flux from a halogen lamp for enhancing Infrared thermography simulation,» International Journal of Heat and Mass Transfer, vol. 256, p. 127961, 2026.

[17] Y. Kim, E. S. Choi, W. Kwak, and Y. Shin, «Analysis of the Thermal Distribution by Using Laser-Beam Irradiation,» Journal of Korean Physical Society, vol. 51, p. 503, 2007.

[18] Y. Zhou, H. Lu, G. Wang, J. Wang, and W. Li, «Voxelization modelling based finite element simulation and process parameter optimization for Fused Filament Fabrication,» Materials & Design, vol. 187, p. 108409, 2020.

[19] S. Monteix, F. Schmidt, Y. Le Maoult, R. Ben Yedder, R. W. Diraddo, and D. Laroche, «Experimental study and numerical simulation of preform or sheet exposed to infrared radiative heating,» Journal of Materials Processing Technology, vol. 119, no. 1, pp. 90–97, 2001.